RESEARCH ARTICLE SUMMARY

ORGANIC CHEMISTRY

Photocatalyzed oxidative cleavage of alkenes using CO_2 as an oxygen donor

Yuman Qin, Peng Ren, Jun Hu, Suman Pradhan, Thanh Huyen Vuong, Xiufang He, Lulu Alluhaibi, Nils Rockstroh, Susanna Monti, Giovanni Barcaro, Aleksander Jaworski, Piotr Kuśtrowski, Jabor Rabeah, Daniel Hohenberger, Sergey Bagnich, Anna Köhler, Josef Breu, Gianvito Vilé, Matthias Beller*, Shoubhik Das*

Full article and list of author affiliations: https://doi.org/10.1126/science.aed6068

INTRODUCTION: Photocatalytic oxidative cleavage of carbon–carbon double bonds to generate oxygenated products is an important class of reactions in organic synthesis. Conventional methods typically rely on stoichiometric oxidants or molecular oxygen, leading to excessive waste generation and safety concerns that are associated with the high oxidizing power or flammability of these reagents. By contrast, carbon dioxide (CO_2), an abundant and oxygen-rich feedstock, represents an attractive alternative for a safer, more sustainable oxidation strategy. However, the exceptionally strong C=O bonds of CO_2 (bond dissociation energy ≈ 179 kcal mol^{-1}) severely limit its activation, and reported examples generally require harsh conditions. As a result, photocatalytic oxidative C=C bond cleavage using CO_2 under mild conditions remains largely unexplored.

RATIONALE: We hypothesized that an iron-based heterogeneous photocatalyst supported on modified carbon nitride could promote CO_2 activation through chemisorption, inducing a distortion of CO_2 from its linear geometry to a bent configuration. This structural perturbation substantially lowers the energetic barrier for C=O bond cleavage of CO_2 under photocatalytic conditions. Coupled with a proton-assisted electron-transfer pathway, this strategy enables CO_2 activation at room temperature and atmospheric pressure. During this process, Fe-bound oxygen species generated upon CO_2 activation act as reactive oxidants, transferring oxygen to alkene C=C bonds coordinated to the Fe centers to form epoxide intermediates. Subsequent ring opening affords diol intermediates, which then undergo C–C bond extension and cleavage. A final oxidation step yields the corresponding ketones or carboxylic acids.

RESULTS: Systematic reaction-condition screening identified $CHCl_3$ as an effective proton source. Under the optimized conditions, 45 substrates, including activated alkene, unactivated alkene, and complex alkenes, were efficiently converted to corresponding ketone or carboxylic acid by using CO_2 as the sole oxygen donor. Notably, high compatibility was observed for functional groups that are typically sensitive to strong oxidative conditions, including aldehydes, hydroxyl groups, and alkynes. Isotopic labeling experiments using $C^{18}O_2$ demonstrated that the oxygen atoms incorporated into the products originated from CO_2. Intermediate-capture studies, combined with in situ diffuse reflectance infrared Fourier transform spectroscopy, revealed a stepwise pathway involving epoxide and diol intermediates before C–C bond cleavage. Extensive characterization of fresh and recycled photocatalysts by STEM, solid-state NMR, XPS, XRD, FTIR, in situ EPR, and x-ray absorption spectroscopy showed minimal structural changes, confirming the robustness of the catalyst. Advanced quantum mechanical simulations further supported the proposed reaction pathway and thermodynamic feasibility.

CONCLUSION: This study establishes a robust heterogeneous photocatalytic platform for oxidative C=C bond cleavage using CO_2 as the sole oxygen source under mild conditions, providing a practical alternative to traditional oxidative cleavage methods. By integrating CO_2 activation and iron-centered oxygen transfer, the approach overcomes the intrinsic thermodynamic stability of CO_2 and transforms it from a one-carbon (C_1) feedstock into an active oxygen source, opening potential opportunities for sustainable photocatalytic oxidation reactions and CO_2 utilization in organic synthesis. □

*Corresponding author. Email: matthias.beller@catalysis.de (M.B.); shoubhik.das@uni-bayreuth.de (S.D.) Cite this article as Y Qin. *et al.*, *Science* **392**, eaed6068 (2026). DOI: 10.1126/science.aed6068

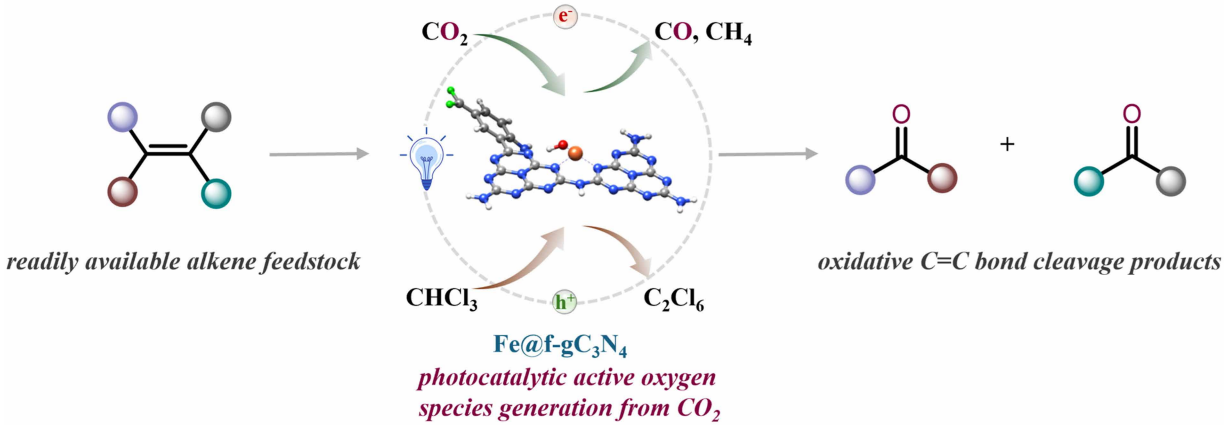

Iron-based heterogeneous photocatalytic C=C bond oxidative cleavage by oxygen abstraction from CO_2.

ORGANIC CHEMISTRY

Photocatalyzed oxidative cleavage of alkenes using CO_2 as an oxygen donor

Yuman Qin[1], Peng Ren[2], Jun Hu[1], Suman Pradhan[1], Thanh Huyen Vuong[3], Xiufang He[4], Lulu Alluhaibi[5], Nils Rockstroh[3], Susanna Monti[6], Giovanni Barcaro[7], Aleksander Jaworski[8], Piotr Kuśtrowski[9], Jabor Rabeah[10,3], Daniel Hohenberger[1], Sergey Bagnich[11], Anna Köhler[11], Josef Breu[1], Gianvito Vilé[4], Matthias Beller[3]*, Shoubhik Das[1]*

Oxidative cleavage of carbon-carbon double bonds often requires hazardous reagents and demanding conditions. In this study, we report a photocatalytic oxidative cleavage of alkenes using benign carbon dioxide (CO_2) as an oxygen donor, producing ketones or carboxylic acids at atmospheric pressure and room temperature. A robust iron-based heterogeneous photocatalyst facilitates oxygen transfer to form an epoxide intermediate that subsequently undergoes ring opening and carbon-carbon bond cleavage to yield the oxidative products with high selectivity. Comprehensive mechanistic studies combine time-resolved spectroscopy, isotope labeling, and in situ spectroscopic analyses with advanced quantum mechanical simulations. These results uncover fundamental principles of oxygen transfer from CO_2 under photocatalytic conditions, offering a sustainable platform for light-driven oxidative transformations.

Oxidation reactions are among the most fundamental and widely utilized transformations in organic synthesis, accounting for nearly 30% of total output in the chemical industry (*1*). Among various oxidative strategies, the oxidative cleavage of alkenes stands out as particularly valuable for generating oxygen-rich compounds, owing to the abundance and ready availability of alkenes as feedstocks (*2*). Traditionally, ozonolysis has been a widely adopted method for this transformation. However, it involves the use of stoichiometric amounts of ozone, a toxic and explosive molecule that introduces serious safety concerns (Fig. 1A) (*3*–*5*). Alternatively, the Lemieux-Johnson oxidation and related osmium-based methods are well-established but require stoichiometric amounts of heavy metals, leading to substantial generation of toxic waste (*6*–*8*). Although molecular oxygen (O_2) represents a greener alternative, oxygen-rich environments enhance flammability, posing risks for large-scale or industrial applications (*9*–*12*). Furthermore, the industrial safety assessments have shown that even minor ignition can trigger rapid fire escalation or explosion under uncontrolled conditions (*13*). To address these challenges, chemists have sought to identify safer and more sustainable oxidants. In this context, the groups of Leonori (*14*) and Parasram (*15*) independently developed elegant oxidative cleavage methods using stoichiometric amounts of nitroarenes under purple-light irradiation. Although effective, these methods still rely on stoichiometric oxidants, resulting in equimolar waste generation. Furthermore, many nitroarene derivatives are toxic and environmentally persistent, limiting their applicability in green synthesis. Therefore, the development of a selective, efficient, and eco-friendly oxidative strategy using a green and safe oxidant remains a pressing challenge in modern synthetic chemistry (*16*).

CO_2 is widely recognized as a nontoxic and safe compound and has been extensively explored as a sustainable one-carbon (C_1) feedstock for the synthesis of fine chemicals. In most cases, CO_2 is transformed into fuels and other products through C-centered species, typically generated either through reduction to a radical anion or through nucleophilic attack (*17*–*24*). Beyond its roles as a carbon source, CO_2 possesses an inherently oxygen-rich composition. If its oxygen atoms could be effectively harnessed under ambient conditions, specifically at atmospheric pressure and room temperature, it could serve as one of the greenest and safest oxidants available for organic synthesis. However, achieving such oxygen transfer remains highly challenging because CO_2 is a thermodynamically stable molecule [Gibbs free energy ($\Delta G°$) ≈ −94.6 kcal mol^{-1}], arising from its fully oxidized carbon center and strong C=O bonds (bond dissociation energy ≈ 179 kcal mol^{-1}) (*25*). Consequently, substantial energy input is required to cleave the C=O bond, which largely explains why CO_2 is rarely used as an oxidant in conventional chemical transformations, in contrast to more reactive oxygen sources such as O_3 (O–O bond dissociation energy ≈ 70 kcal mol^{-1}) (*26*). A recent breakthrough demonstrated the photodissociation of CO_2 into carbon and molecular oxygen (O_2) under vacuum-ultraviolet (VUV) irradiation (Fig. 1B) (*27*). Although these findings provide critical mechanistic insights, the requirement of high-energy VUV light limits their practical application in synthetic chemistry. Alternatively, plasma-based CO_2 splitting [operating at 150 to 300 root mean square voltage (V_{rms}) and −25°C] has been applied to the epoxidation of stilbene. However, this approach remains energy-intensive, requires specialized equipment, and lacks definitive confirmation, such as $C^{18}O_2$-labeling experiments verifying that the oxygen atoms incorporated into the products originated from CO_2 (*28*). In another approach, He and co-workers developed an electrocatalytic CO_2 reduction method using a nanoscale cobalt catalyst and a lithium metal anode. In this system, CO_2 is first converted into Li_2CO_3 and Li_2O, and subsequent oxidation of Li_2O releases O_2. Despite its effectiveness, the strategy relied on highly reactive lithium and was incompatible with aqueous environments, restricting its broader applicability (*29*). Notably, Antonietti and co-workers reported the oxidation of benzene (112.2 mmol) to phenol (0.26 mmol) using mesoporous carbon nitride (mpg-C_3N_4) as the catalyst under 10 bar of CO_2 at 150°C in the presence of triethylamine (1.98 mmol). Under these conditions, a benzene conversion of 20% and a phenol selectivity of 65% (based on triethylamine) were obtained, corresponding to an overall phenol yield of 0.2% when calculated with respect to benzene. Although no $C^{18}O_2$-labeling experiments were performed to confirm the oxygen source in phenol, this study nonetheless provided an important early example of using CO_2 as an oxidant in the context of organic synthesis (*30*). Despite these advances, the direct capture and incorporation of oxygen atoms from CO_2 in valuable organic transformations under synthetically practical conditions remains a major challenge.

We became interested in developing a photocatalyst capable of applying CO_2 as a safe oxidant under atmospheric pressure and room temperature. In this context, a heterogeneous photocatalyst was ideal because of its recyclability and high stability (*31*–*35*). However, the choice of metal center and support material plays a crucial role in optimizing reactivity and selectivity within this class of catalysts (*36*). Polymeric carbon nitride (PCN) stands out in this regard, owing to its

[1]Department of Chemistry, University of Bayreuth, Bayreuth, Germany. [2]Shanxi Key Laboratory of Catalysis and Energy Coupling, College of Chemical Engineering and Technology, Taiyuan University of Science and Technology, Taiyuan, China. [3]Leibniz-Institut für Katalyse e. V., Rostock, Germany. [4]Department of Chemistry, Materials and Chemical Engineering "Giulio Natta," Politecnico di Milano, Milan, Italy. [5]National Synchrotron Radiation Centre SOLARIS, Jagiellonian University, Kraków, Poland. [6]CNR-ICCOM, Institute of Chemistry of Organometallic Compounds, Pisa, Italy. [7]CNR-IPCF, Institute for Chemical and Physical Processes, Pisa, Italy. [8]Department of Chemistry, Stockholm University, Stockholm, Sweden. [9]Faculty of Chemistry, Jagiellonian University, Kraków, Poland. [10]State Key Laboratory of Low Carbon Catalysis and Carbon Dioxide Utilization, Lanzhou Institute of Chemical Physics (LICP), Chinese Academy of Sciences, Lanzhou, P. R. China. [11]Department of Physics, University of Bayreuth, Bayreuth, Germany. ***Corresponding author. Email: matthias.beller@catalysis.de (M.B.); shoubhik.das@uni-bayreuth.de (S.D.)**

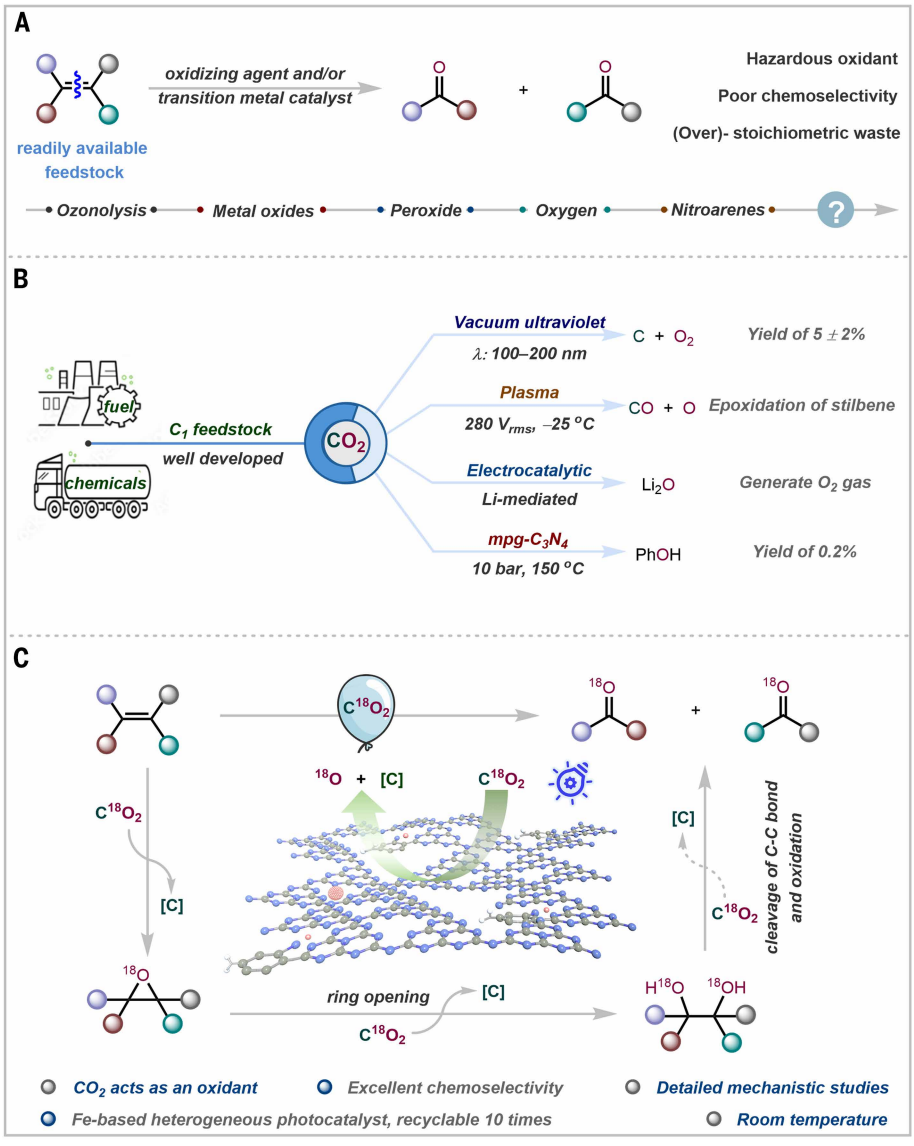

Fig. 1. Cleavage of C=C double bonds. (**A**) Oxidative cleavage of aliphatic alkenes. (**B**) CO_2 transformation as C_1 feedstock or "O" source. (**C**) This work: Fe-based heterogeneous photocatalyst for selective oxidative cleavage of alkenes, using CO_2 as the sole oxygen source.

exceptional thermal stability, nitrogen-rich architecture, and tunable electronic properties, for use as a valuable support in diverse reactions (*37*–*39*). With these features in mind, we focused on designing a Fe-based heterogeneous photocatalyst using PCN as the support. Iron is naturally abundant, readily accesses multiple redox states, and exhibits strong oxophilicity—characteristics that make it particularly suited for oxygen transfer reactions (*40*–*42*). Moreover, iron-oxygen complexes supported by electron-deficient ligands have demonstrated remarkable reactivity in oxidative transformations under an oxygen atmosphere (*43*). On the basis of these precedents, we hypothesized that a Fe-based heterogeneous photocatalyst with an electron-deficient coordination environment should favor interaction with the oxygen atom of CO_2 over carbon, thereby promoting selective CO_2 activation. Although the overall free energy for direct CO_2 splitting is thermodynamically uphill ($\Delta G^\circ \approx 62$ kcal mol^{-1}), efficient chemical adsorption of CO_2 on a Fe site is expected to distort its linear geometry into a bent configuration, substantially lowering the energy barrier for CO_2 activation (*44*, *45*). Moreover, a proton-assisted approach further reduces the thermodynamic barrier (*46*). The cooperative interaction should facilitate the generation of Fe-bound oxygen species capable of transferring oxygen to C=C bonds in alkenes, forming epoxide intermediates (Fig. 1C). Subsequent ring-opening and β-scission processes would then afford the corresponding carbonyl compounds through oxidative cleavage. Following this rationale, we developed a Fe-based heterogeneous photocatalyst, Fe@f-gC_3N_4, which exhibits high selectivity in the oxidative cleavage of alkenes by using CO_2 as a green and mild oxidant. Notably, $C^{18}O_2$-labeling experiments provided direct and unambiguous evidence that the oxygen atoms incorporated into the products originated from CO_2. Furthermore, mechanistic investigations combined with advanced quantum mechanical calculations provide strong substantial support for the proposed reaction pathway and emphasize the pivotal role of CO_2-derived oxygen species in enabling this transformation.

Catalyst development

At the beginning of this project, Fe@f-gC_3N_4 was synthesized through a two-step process involving successive impregnation and calcination (fig. S1). To create an electron-deficient environment, 2-amino-5-(trifluoromethyl) benzonitrile was introduced into the PCN support. After this synthesis, the electronic band structure was probed using ultraviolet-visible (UV-vis) diffuse reflectance spectroscopy (DRS) in conjunction with Mott-Schottky measurement (figs. S2 and S3). The band gap was calculated to be 2.63 eV according to the Tauc plot, and the positive slope observed in the Mott-Schottky curve indicated the *n*-type semiconducting behavior of Fe@f-gC_3N_4. In general, the bottom potential of the conduction band (CB) for an *n*-type semiconductor is considered to have a similar value to flat band potential (E_{fb}). Therefore, the conduction band potential (E_{cb}) was estimated to be –1.39 V [versus saturated calomel electrode (SCE)]. Accordingly, the valence band (VB) of Fe@f-gC_3N_4 was at ~+1.24 V (versus SCE). Furthermore, the elemental composition of the catalyst was characterized by using CHN elemental analysis, inductively coupled plasma optical emission spectrometry (ICP-OES), and solid-state nuclear magnetic resonance (NMR) spectroscopy. The N, C, and H contents were found to be 57.30, 32.92, and 1.82 wt %, respectively, and the iron content was determined to be 0.143 wt % [see detailed procedure in supplementary materials (SM), sections 3 and 4]. According to quantitative analysis, the fluorine content in the Fe@f-g-C_3N_4 catalyst was estimated to be 0.027 wt % (fig. S39). Next, Fe@f-gC_3N_4 was applied to *trans*-β-methylstyrene (**1a**) for the oxidative cleavage reaction at room temperature under CO_2 atmosphere (balloon) and visible light irradiation (Kessil lamp, λ= 456 nm).

Careful optimization of reaction parameters revealed that **1a** and Fe@f-gC_3N_4 (5 mg, 0.064 mol % Fe) in a mixed solvent of $CHCl_3$ (0.6 ml) and MeCN (1.4 ml) provided the desired benzoic acid (**2a**) in 82% yield within 24 hours. The commonly used proton donors resulted in markedly lower yields of **2a** (table S2, entries 5 to 9). This decrease is attributed to the formation of radical cations from these proton donors,

which competitively quench the oxygen species derived from CO_2, thereby suppressing the oxidative cleavage of **1a**. By comparison, $CHCl_3$ can serve as a proton source without consuming the CO_2-derived oxygen species, leading to efficient product formation. Control experiments were also performed to assess the role of each of the reaction components under optimized conditions (table S2, entries 36 to 38) and revealed that the synergistic interplay of Fe@f-gC_3N_4, CO_2, $CHCl_3$, MeCN, and light was essential to achieve an efficient oxidative cleavage of C=C bond in *trans*-β-methylstyrene. Notably, using f-gC_3N_4, Fe@gC_3N_4, and C_3N_4 under the identical conditions resulted in a considerably reduced yield, highlighting the critical role of iron in the catalytic process (table S2, entries 33 to 35). Subsequently, the stability of the photocatalyst was evaluated through 10 consecutive recycling experiments. After each reaction, the Fe@f-gC_3N_4 catalyst was readily recovered by centrifugation, followed by washing and drying. The catalyst maintained high catalytic activity over 10 cycles, with the yield of **2a** decreasing only slightly from 82 to 70%, demonstrating good catalytic stability (see detailed information in section 6.4 in supplementary materials). Furthermore, the x-ray diffraction (XRD) (fig. S36) patterns and Fourier transform infrared (FTIR) spectra (fig. S37) of the fresh and recycled Fe@f-gC_3N_4 catalysts showed no appreciable differences, indicating that the catalyst structure remained stable throughout the recycling process. In addition, under continuous-flow conditions, the immobilized photocatalyst was irradiated for more than 21 days and, after recovery, afforded a similar yield (80%) to that of the fresh catalyst (82%), demonstrating excellent long-term photostability. Lastly, iron leaching tests confirmed the heterogeneous nature of the photocatalytic system (fig. S9).

Reaction scope

As a result of our successful optimization studies, we explored the generality of the C=C bond cleavage protocol (Fig. 2). Although olefin motifs in some substrates (**1q**, **1x**, **1y**, **1ah**, **1an**, **1av**, **1ax**, **1az**, **1bb**; see section 6.8 in SM) were accessed from the corresponding ketones through established olefination reactions, these examples were included as proof-of-concept studies to assess the robustness and late-stage functional-group tolerance of this C=C bond cleavage strategy. A variety of olefins were selectively converted into the corresponding products with high efficiency. First, 1,2-disubstituted alkenes were investigated: Compared with *trans*-β-methylstyrene (**1a**), substrates bearing electron-donating groups (EDGs) such as −OMe exhibited enhanced reactivity, delivering the final product in 85% yield (**2b**) in 16 hours. Monosubstituted styrene derivatives demonstrated excellent functional compatibility. For example, styrenes substituted with an EDG such as −Me or −OMe provided the desired products in 63 to 65% yield (**2c** to **2e**). In addition, substrates bearing electron-withdrawing groups (EWGs), including $-CF_3$, −COOH, and −Cl moieties, were also compatible, generating the products in 58 to 62% yield (**2f** to **2h**). Notably, extending the reaction time from 24 to 48 hours did not lead to a major improvement in yield for either class of substrates. This behavior can be attributed to a pronounced decrease in reaction rate as the substrate concentration diminishes over time, coupled with partial decomposition of the starting materials under prolonged irradiation, which together limit further product formation. Further expansion of the scope toward α-methylstyrenes showed that substrates containing EDG (−^{t}Bu, −OMe, and −OH) produced the corresponding ketones in 71 to 90% yield (**2i** to **2l**). The halogenated (−F, −Cl, −Br) and nitro-substituted ($-NO_2$) substrates were smoothly converted into their respective ketones in 53 to 65% yield (**2m** to **2p**). Additionally, various branched-chain alkenes were compatible with the reaction condition, yielding the corresponding ketones in good to excellent yields (50 to 95%, **2q** to **2u**). In the case of dienes, both of the C=C bonds underwent oxidative cleavage efficiently to provide the desired product (**2v**). Furthermore, heteroaromatics including pyridine- (**2w**), thiophene- (**2x**), and furan-substituted alkenes (**2y**) also reacted smoothly, affording the corresponding products in 68 to 71% yield. This oxidative transformation was further extended to the tetrasubstituted alkene diethylstilbestrol and the cyclic alkene indene, delivering the desired ketone in 65 and 55% yield, respectively (**2z** and **2aa**). To further probe the chemoselectivity of the reaction, substrates bearing potentially oxidizable functional groups such as alcohol (**2ab**), aldehyde (**2ac**), and alkyne (**2ad**) were examined. The oxidation occurred selectively at the C=C bond when these functionalities were positioned distal to the alkene. This selectivity is attributed to preferential alkene coordination to the catalytically active Fe site, which enables alkene activation, whereas other functional groups remain kinetically inaccessible under these photoredox conditions. Furthermore, nonactivated alkenes, including aliphatic alkenes bearing biologically relevant functionalities such as carboxylic acid ester (**2ae**), phthalimide (−Nphth, **2af**), and silylether (−OTIPS, **2ag**), were also compatible and afforded the corresponding ketones in 68 to 73% yield. Even unfunctionalized linear aliphatic alkenes provided the oxidative cleavage product with a high yield (75%, **2ah**). Next, exocyclic alkenes were converted into desired ketones in 55 to 70% yield (**2ai** to **2al**). Increasing the ring size to 8- and 12-membered rings did not hamper the reaction efficiency (**2am** and **2an**). Notably, even strained small-ring substituted olefins underwent selective oxidation to ketones (**2ao** and **2ap**) in good yields (60 to 63%). Moreover, aliphatic alkenes bearing amino acid functionalities were successfully transformed (**2aq** and **2ar**) into ketones in good yields (59 to 63%), suggesting potential application of this method for peptide and protein modifications.

Expanding the scope further, we found that 1,2-disubstituted aliphatic alkenes were also suitable substrates, yielding the corresponding carboxylic acids (**2as** and **2at**) in moderate yield (41 to 45%). The reduced efficiency in these cases is attributed to increased acidity of the reaction medium arising from carboxylic acid formation, which promoted partial decomposition of the unreacted starting materials. Given the mild reaction conditions and broad functional group compatibilities of this approach, we envisioned that it could serve as a powerful tool for modifying complex molecules. Ozonolysis is frequently used in medicinal chemistry as well as in synthetic chemistry for the cleavage of C=C bonds. However, owing to the extreme oxidizing power of ozone, protection and subsequent deprotection of oxidizable functional groups are often required. By contrast, our strategy allows a chemoselective approach for the cleavage of C=C bonds under mild conditions and in turn avoids these protection and subsequent deprotection steps. Fenofibrate (**2au**) and donepezil (**2av**) were efficiently obtained from their corresponding alkene precursors. Moreover, triprolidine (**2aw**), a widely used antihistamine, was converted into the corresponding ketone with excellent efficiency. Beyond these examples, derivatives of loxoprofen (**2ax**), haloperidol (**2ay**), ezetimibe ketone (**2az**), estrone (**2ba**), and epiandrosterone (**2bb**) were also obtained in good yields, underscoring the high synthetic utility of this protocol for modifying bioactive molecules. Taken together, these results clearly demonstrate that this soft-oxidation approach is very selective and can be effectively applied to complex molecules even in the presence of sensitive oxidizable functional groups. Having demonstrated the generality of this protocol, we carried out gram-scale conversion of **1a** (details in section 6.6 of SM). Benzoic acid was obtained in 75% yield from a 5-mmol scale reaction and 73% yield from a 10-mmol scale reaction. Furthermore, the procedure was successfully scaled up using a continuous flow setup (fig. S10). With a retention time of t_R = 20 min, benzoic acid was obtained in 70% yield from a 10-mmol scale reaction.

Further catalyst characterization

We subjected the as-synthesized Fe@f-gC_3N_4 to a series of characterization techniques to gain deeper insights into its structural and electronic properties. Initially, to confirm the presence of iron species on the modified g-C_3N_4 support, the photocatalyst was subjected to chemical mapping through high-angle annular dark-field scanning transmission

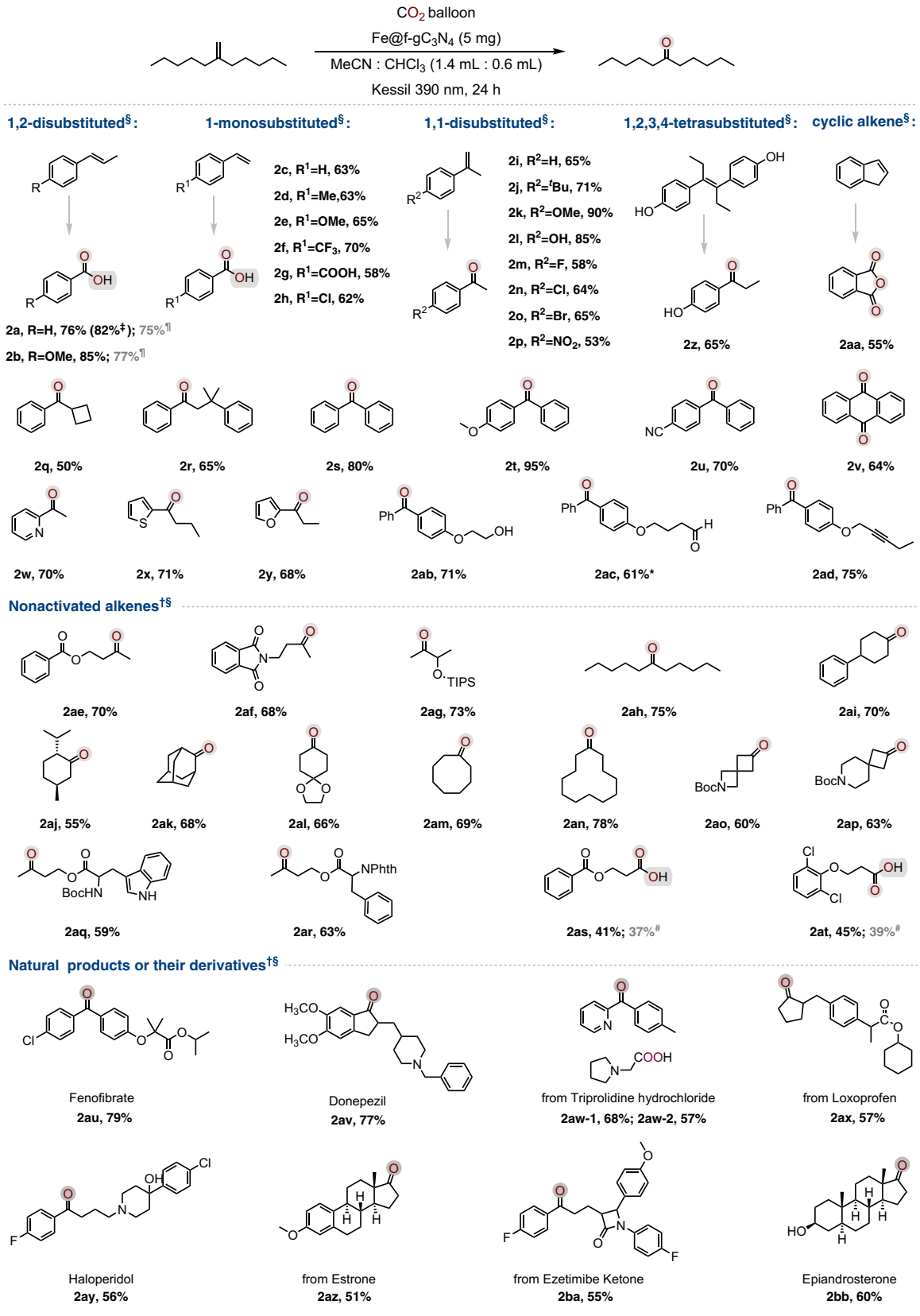

Fig. 2. Substrate scope of the oxidative cleavage. Reaction conditions: alkene (0.2 mmol, 1 equiv.), Fe@f-gC_3N_4 (5 mg, 0.064 mol % Fe), $CHCl_3$ (0.6 mL), MeCN (1.4 mL), CO_2 (balloon), irradiated under Kessil lamp ($\lambda = 456$ nm), room temperature; *reaction at 0°C; †irradiated under Kessil lamp ($\lambda = 390$ nm); ‡^{1}H NMR yield; §isolated yield; ¶gas chromatography–flame ionization detection (GC-FID) yield of acetic acid; #GC-FID yield of propionic acid.

electron microscopy (HAADF-STEM) coupled with energy-dispersive x-ray (EDX) spectroscopy. HAADF-STEM imaging clearly identified Fe-containing nanoparticles dispersed over the modified g-C_3N_4 support in the photocatalyst (Fe@f-gC_3N_4). The EDX spectra of the photocatalyst indicated the presence of iron in oxide form (fig. S31). Furthermore, the analysis confirmed a high contrast for specific sites, indicating single-atom dispersed Fe (highlighted by red arrows in Fig. 3B and fig. S32) around the nanoparticle counterparts and surface-enriched iron species (highlighted by cyan and blue arrows independently in fig. S32). Similar results were obtained from the catalyst after 160 hours of photooxidation of **1a** (figs. S33 and S34). Subsequently, x-ray photoelectron spectroscopy (XPS) analysis provided further insight into the surface composition of Fe@f-gC_3N_4 (fig. S35) before and after the photocatalytic reaction. The fresh material showed the g-C_3N_4 phase as the main surface component, identified by a peak at 288.1 eV in the C 1s region (fig. S35A), assigned to sp^2-bonded carbon (N-C=N), as well as three peaks in the N 1s region (fig. S35B) at 398.6 eV (N in C-N=C), 400.0 eV [bridging N in N–$(C)_3$], and 401.1 eV (N in =NH and –NH_2 groups), respectively (*47*, *48*). The determined N/C atomic ratio of 1.21 is slightly lower than the stoichiometry expected. Furthermore, Fe-containing species were found in the Fe 2p region (fig. S35C). The multiplet peak at 710.5 eV corresponded to the presence of FeO_x, whereas the additional peak at 706.6 eV confirmed the occurrence of dispersed metallic Fe species as well. The relative areas of the fitted components indicated that the ratio of metallic to oxidized Fe species was ~0.37. The Brunauer–Emmett–Teller surface area was determined to be 7.0 $m^2\ g^{-1}$, indicating the nonporous nature of the Fe@f-gC_3N_4 material (fig. S38).

To gain further insight into the local structure of the photocatalyst and to investigate any potential structural changes upon material doping with Fe ions, solid-state NMR spectra of all NMR-active nuclei present in the material (^{1}H, ^{13}C, ^{15}N, and ^{19}F) were collected to probe the chemical structure of the functionalized graphitic carbon nitrides (Fig. 3, E to H). The overall chemical structure and polymerization degree were not affected by doping with Fe ions to any great extent (*49*). Decrease of the ^{1}H NMR signal intensity of the terminal (surface) –NH_2 groups in relation to bridging >NH groups in the spectrum of Fe@f-gC_3N_4 catalyst (compared with parent f-gC_3N_4 material; Fig. 3E) could be attributed to paramagnetic effects due to the presence of Fe ions at the material surface. The functionalization of the graphitic carbon nitride with the fluorinated reagent was evidenced by the ^{19}F magic-angle spinning (MAS) NMR spectrum shown in Fig. 3H. However, although the precursor contained a –CF_3 group, the observed ^{19}F NMR shift of –104 ppm was more negative than expected from the –CF_3 moiety (~–63 ppm). The shift was not affected by doping of the material with Fe ions, so to uncover the chemical nature of this signal, hypothetical models shown in fig. S40 were evaluated with quantum chemistry methods. Ab initio calculations of ^{19}F NMR shifts suggested that for the model containing a –CF_3 group (fig. S40A), the obtained shift of –63 ppm matched exactly that expected for trifluoromethylbenzene, which confirmed the robustness of the theoretical method and the model but could not explain the experimentally observed signal at –104 ppm. By contrast, calculated ^{19}F NMR shifts of –80 and –124 ppm for the models representing =CF_2 and –CHF_2 scenarios (fig. S40, B and C, respectively) encompassed the experimental result. Shifts obtained for the –CH_2F group and the ArF moiety (fig. S40, D and E) were –209 and –131 ppm, respectively, thus more negative. Although none of the considered models provided an ^{19}F NMR shift that matched exactly the experimentally

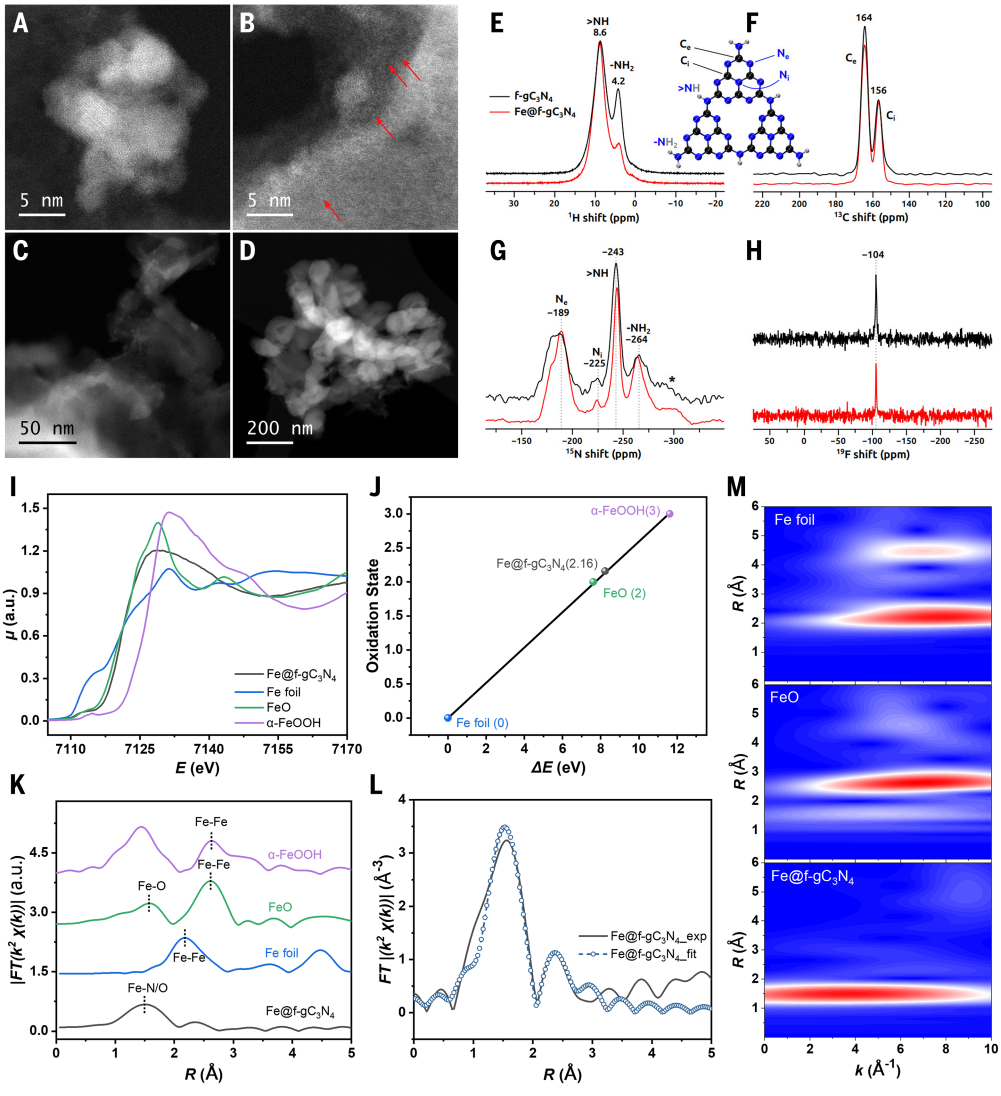

Fig. 3. Characterization results of Fe@f-gC_3N_4 photocatalyst. (**A** to **D**) Selected HAADF-STEM images of Fe@f-gC_3N_4 at different magnifications. (**E**) Solid-state ^{1}H magic-angle spinning (MAS) NMR spectra. (**F**) ^{13}C cross-polarization magic-angle spinning (CPMAS) NMR spectra. (**G**) ^{15}N CPMAS NMR spectra. Spinning sideband in (G) is marked with an asterisk. (**H**) ^{19}F MAS spectra collected from the f-gC_3N_4 material and Fe@f-gC_3N_4 catalyst. (**I**) Normalized Fe K-edge XANES spectra. (**J**) Valence of various Fe species obtained from Fe K-edge XANES spectra. (**K**) k^3-weighted FT spectra of Fe in R space. (**L**) Corresponding fitting curves of FT-EXAFS spectra of Fe@f-gC_3N_4 in R space; coefficient of determination (R^2) = 0.015. (**M**) Wavelet transforms of the k^3-weighted EXAFS spectrum of Fe foil, FeO, and Fe@f-gC_3N_4, respectively.

observed signal at −104 ppm, our theoretical results strongly suggested that the precursor in the trifluoro form ($-CF_3$) underwent partial defluorination and was present in the material in a difluoro motif, similar to $=CF_2$ or $-CHF_2$, but not in the monofluoro motif ($-CH_2F$ or ArF).

Furthermore, x-ray absorption spectroscopy (XAS) was used to investigate the local Fe environment in the samples before and after photocatalytic reactions (*50*, *51*). The normalized x-ray absorption near-edge structure (XANES) spectra at the Fe K-edge are presented in Fig. 3I. A distinct pre-edge feature, observed in the 7110-to-7120-eV range, corresponds to the 1s-to-3d orbital transition of Fe, which is accompanied by ligand-to-metal charge transfer (*52*, *53*). For comparison, we analyzed Fe@f-gC_3N_4 alongside reference spectra from Fe foil, FeO, and α-FeOOH. The absorption edges of both Fe@f-gC_3N_4 and postreaction Fe@f-gC_3N_4 were found to be close to those of FeO and placed between those of α-FeOOH and Fe foil. Notably, no difference between the Fe@f-gC_3N_4 and postreaction Fe@f-gC_3N_4 samples was observed (fig. S41), suggesting that the catalyst maintained structural stability throughout the reaction. Linear regression analysis of the zero-crossing point in the first-order derivative confirmed that the oxidation state of Fe was ~+2.16 for both Fe@f-gC_3N_4 and postreaction Fe@f-gC_3N_4 samples (Fig. 3J). Fourier-transform extended x-ray absorption fine-structure (FT-EXAFS) spectra in the R space (without phase correction) are shown in Fig. 3K. The FeO sample displayed a predominant peak at ~1.56 Å, corresponding to the Fe–O bond, and another peak at around 2.62 Å, attributed to the Fe–Fe bond. Both FT-EXAFS spectra of Fe@f-gC_3N_4 and postreaction Fe@f-gC_3N_4 (as seen in Fig. 3K and fig. S41) revealed a similar profile, with a major peak near 1.48 Å, which was attributed to Fe-N/O species. To further examine the coordination of the Fe sites in the catalysts, quantitative EXAFS fitting was performed as depicted in Fig. 3K, fig. S41, and table S7. The EXAFS fitting was conducted with a model of cubic FeO, and the first and second scattering paths included Fe-O and Fe-Fe. The results indicated that the main EXAFS contribution arises from Fe–N/O bonds, which are located at 2.03 Å, consistent with the theoretically calculated Fe–O bonds (2.13 Å). However, the coordination number of Fe-Fe was much smaller than that of FeO, suggesting that the prepared Fe@f-gC_3N_4 consisted of a mixture of atomically dispersed Fe species and Fe oxide nanoparticles. Furthermore, the postreaction Fe@f-gC_3N_4 sample presented changes compared with the pristine sample. In particular, the white-line intensity increased, along with the appearance of a peak at ~5.5 Å in EXAFS, indicating the formation of aggregated Fe oxide species after the reaction. Given that the wavelet transform (WT) offers strong resolution in both K and R space, the EXAFS oscillation at the Fe K-edge was further analyzed, as shown in Fig. 3L. The WT contour plots for Fe@f-gC_3N_4 exhibit intensity maxima at 1.48 Å, corresponding to Fe–O/N coordination, reinforcing the above findings. The surface concentration of Fe in Fe@f-gC_3N_4 was too low to display characteristic signals by Mössbauer spectroscopy (details in section 6.2 of SM).

Mechanistic investigation

To investigate the mechanism of the reaction, time-course experiments were conducted under optimized conditions. Notably, the formation of epoxide and benzaldehyde was observed after 6 hours, and they reached their maximum yield (49 and 30%, respectively) within the first 12 hours. Subsequently, benzoic acid began to form after 18 hours and continued to accumulate, reaching its highest yield of 82% after 24 hours (figs. S12 and S13). This behavior reflects the role of benzaldehyde as an in situ–generated, catalyst-bound intermediate. By contrast, preinstalled aldehyde functionalities located remotely from the alkene (e.g., **2ac**) remain intact under the reaction conditions, highlighting that aldehyde compatibility applies to noncoordinating aldehydes rather than reactive intermediates formed at the catalytic site. To probe the origin of the oxygen atoms and product, the reaction was conducted under a $C^{18}O_2$ atmosphere. The results revealed the formation of ^{18}O-labeled epoxide and ^{18}O-labeled benzaldehyde after 6 hours, followed by the formation of ^{18}O-labeled benzoic acid after 24 hours (Fig. 4A; details in section 7.2 of SM). These findings strongly indicated that all of the oxygen atoms in both the intermediates and the final product originated from CO_2. The formation of both CO and CH_4 from CO_2 was observed in head-space gas chromatography (fig. S19). Next, radical quenching and trapping experiments were performed to delineate the reaction pathway (table S4). The addition of 2,2,6,6-tetramethylpiperidine-1-oxyl (TEMPO) completely suppressed the formation of the product, strongly suggesting the involvement of a radical pathway in the oxidative cleavage process. Moreover, reactive oxygen species [Fig. 4B, (II)] derived from CO_2 were successfully captured by using high-resolution mass spectrometry (HR-MS). Concurrently, a

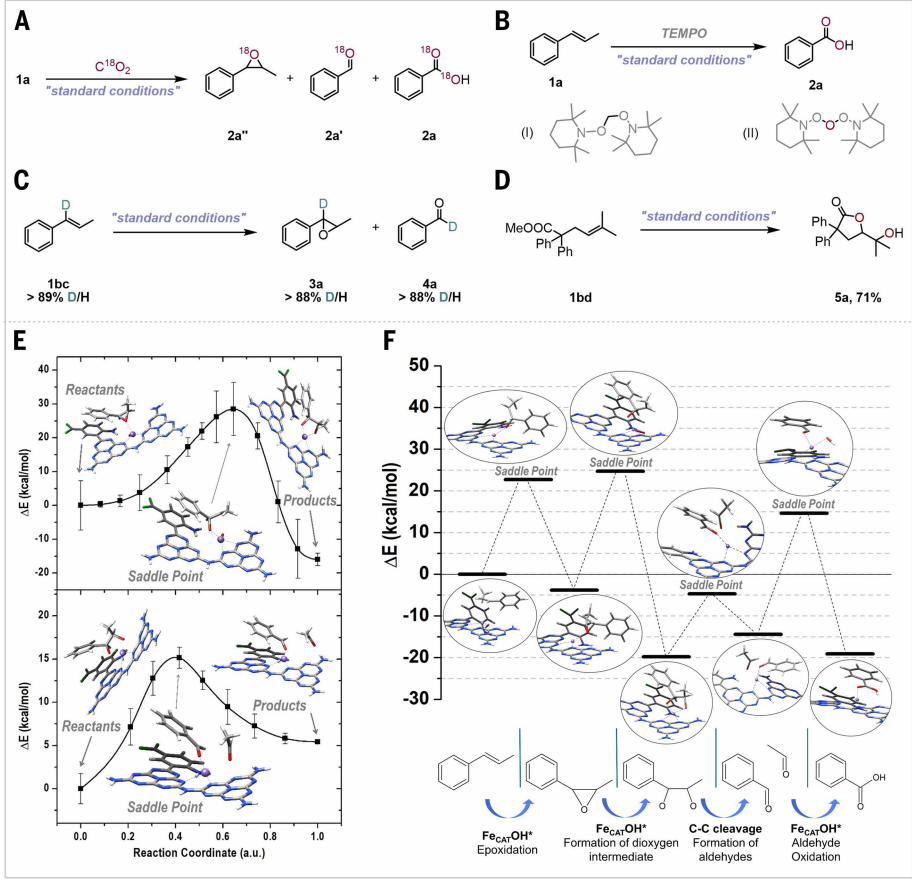

Fig. 4. Mechanistic studies and density functional theory (DFT) calculations. (**A**) $C^{18}O_2$-labeling experiments. (**B**) Intermediate-capture experiments. (**C**) Isotope experiments. (**D**) Cyclization experiments. (**E**) DFT level calculations in solution; the error bars are the uncertainty estimated by the nudged elastic band algorithm during the derivation of the energy profile. (**F**) Sequential thermodynamic scheme of the overall reaction starting from β-methylstyrene adsorbed on the Fe@f-gC_3N_4 through coordination of the C=C bond.

methylene radical–TEMPO adduct [Fig. 4B, (I)] was detected (*54*), correlating with the formation of methane after the reaction. In this process, a CCl_3 radical was also generated, which subsequently underwent homocoupling to form C_2Cl_6 (table S5). The results indicated that $CHCl_3$ served as a hydrogen donor, facilitating the conversion of CO_2 into CH_4. In situ spin-trapping electron paramagnetic resonance (EPR) experiments were performed to further elucidate the behavior of the generated radicals. The detection of DMPO-CCl_3 and DMPO-CH_3, as well as DMPO-OOR spin adducts (figs. S25 and S26), provided direct and compelling evidence for the stepwise formation of methane from CO_2. Additionally, isotope-labeling experiments (Fig. 4C) demonstrated that the hydrogen atom from $CHCl_3$ did not contribute to the formation of key intermediates **4a** or **5a** or the formation of the final product, benzoic acid. To further elucidate the role of $CHCl_3$ in the photocatalytic process, fluorescence quenching experiments were performed (details in section 7.14 of SM). Photoluminescence measurements demonstrated that $CHCl_3$ efficiently quenched the excited state of Fe@f-gC_3N_4. Compared with the alkene (**1a**), $CHCl_3$ exhibited much stronger quenching ability, which clearly indicated that it acted as a primary quencher in this system. This experiment is consistent with the oxidation of a $CHCl_3$ to form CCl_3 radical by holes from the valence band under our photocatalytic reaction conditions. To elucidate the overall reaction stoichiometry, all reactants and products were quantitatively analyzed (details in section 7.8 of SM). As a representative example, substrate **1z** was selected to rigorously track oxygen incorporation and the fate of carbon-containing species. Specifically, consumption of 0.24 mmol of CO_2 and 0.24 mmol of $CHCl_3$ affords 0.06 mmol of CH_4 and 0.18 mmol of CO, accompanied by the formation of 0.12 mmol of C_2Cl_6, in correlation with the production of 0.26 mmol of ketone **2z**. Conversely, stepwise control experiments using epoxide and diol as substrates under the optimized conditions confirmed that epoxide and diol are both reaction intermediates in this oxidative cleavage reaction rather than by-products (details in section 7.10 of SM). Furthermore, the formation of product **6a** (Fig. 4D) suggested that a diol intermediate was also involved in this oxidative cleavage process. The light-on and -off experiments demonstrated the critical role of light in this reaction (fig. S28) and revealed that the reaction ceased entirely in the absence of light and resumed immediately upon further illumination. Moreover, in situ diffuse reflectance infrared Fourier transform spectroscopy further provided evidence for the formation of epoxide intermediates and their subsequent oxidation to carboxylic acids (fig. S30). To further probe the involvement of iron in charge-transfer processes and CO_2 activation, in situ EPR experiments were performed (fig. S27). Under photoirradiation in an argon atmosphere, Fe@f-gC_3N_4 exhibited an increase in CB electrons accompanied by a decrease in the ferromagnetic iron signal. Notably, the decline in ferromagnetic signal occurred more rapidly and markedly in the presence of CO_2. This observation could be attributed either to the oxidation of the ferromagnetic phase to a weakly magnetic phase through the CO_2-mediated process or to spin disorder induced by adsorbed intermediates.

The oxidative cleavage mechanism was further investigated at the quantum mechanical (QM) level with a well-tuned model developed in an earlier study (*49*, *55*). There, we simulated the conversion of CO_2 on the portion of the catalyst composed of iron species entrapped between two melamine subunits and a fluorinated ligand. In the activated configuration, the CO_2 molecule was chemisorbed onto the catalyst. Upon light irradiation, modeled as an h^+/e^- pair transfer, charge excitation triggered elongation of the C–O bond and bending of the O–C–O angle, leading to CO_2 dissociation into CO and an OH species (fig. S42). In the theoretical model (fig.S43), the resulting OH species could either remain adsorbed on the photocatalyst or be released in solution, depending on the surrounding environment. On the basis of these findings, we hypothesized that the catalyst incorporated OH species produced from the CO_2 (fig. S43) and that the β-methylstyrene substrate also coordinated to the catalyst through its C=C bond of the propylene chain, as already observed for similar systems (*56*, *57*). The optimized complexes of the catalyst with the *cis*- and *trans*-methylstyrene configurations shown in fig. S43 were equally stable ($\Delta E = 0.1$ kcal/mol), with similar molecular orientations relative to the melamine framework. The simulations of the UV-vis spectra of these optimized geometries showed that the catalyst-adsorbate complexes had intense absorption bands in the 400-to-475-nm region (fig. S43), which corresponded to the experimental Kessil light emission. The examination of the orbitals involved in the dominant transitions revealed that the photoexcitation could induce electron transfers from the molecule to the catalyst, generating radical species. More specifically, we observed the transfer of the H_{OH} to the catalyst, the elongation of the C=C bond by about 0.11 Å, the connection of the oxygen species to the closest carbon radical, and the formation of the epoxide ring. The comparison of the reaction mechanism barriers of the two molecules displayed in fig. S44 suggested that the first *cis*-epoxide isomer was more favorably converted by ~6 kcal/mol to the final epoxide product, which is in agreement with the experimental finding. Given these results, we focused on the *cis*-epoxide isomer only and simulated the entire conversion process of the epoxide in the presence of a further oxygen atom adsorbed on the photocatalyst as a result of the activation of a second CO_2 molecule. UV-vis excitation simulations confirmed that further light irradiation continued to induce charge transfer from the adsorbate to the catalyst, leading to epoxide ring opening (fig. S45). Indeed, the reaction proceeded via a two-step pathway (Fig. 4E, top): (i) epoxide ring opening followed by migration of the oxygen from the photocatalyst to the carbon radical and (ii) formation of a new C–O bond and ring closure. The epoxide ring opening corresponded to an activation energy of about 29 kcal/mol (*58*). The final product was more stable by about 16 kcal/mol than the initial configuration. The final cyclic complex could be related to the diol intermediate suggested by the experimental observations (Fig. 4D). Analogously to what was observed for the *trans*-β-methylstyrene and the *cis*-epoxide, light irradiation could induce activation of the cyclic complex by a charge transfer from the adsorbate to the catalyst (see simulated UV-vis excitation profile in fig. S46). The subsequent process of C–C cleavage consisted of the progressive elongation of the C–C bond followed by the formation of benzaldehyde, which remained connected to the catalyst. Notably, the C–C cleavage was energetically more favorable than the epoxide ring opening by about 14 kcal mol^{-1}. A possible pathway is shown in Fig. 4E, bottom. Lastly, we simulated the oxidation of the benzaldehyde intermediate to benzoic acid, which required an additional oxygen atom derived from a third CO_2 molecule activation. This transformation exhibited an energy barrier of ~29 kcal mol^{-1} (fig. S47), further supporting a sequential oxygen species transfer mechanism.

On the basis of the experimental results and indications extracted from QM calculations (Fig. 4F shows a possible thermodynamic path, including thermal barriers of direct and reverse reactions), a plausible mechanism summarizing the full oxidative cleavage transformation has been proposed. Upon irradiation, photoexcitation generated a charge separation, leading to electron and hole migration on the Fe@f-gC_3N_4 photocatalyst's surface. $CHCl_3$ acted as cosolvent and a reductant, undergoing oxidation in the valence band to release protons and generating CCl_3 radicals, which dimerized to form hexachloroethane as a by-product. This by-product formation reflected the sacrificial role of $CHCl_3$ and represents a limitation in terms of sustainability. Concurrently, given the presence of abundantly available adsorption sites on the surface of Fe@f-gC_3N_4, the protons released from $CHCl_3$ acted in synergy with the reducing electrons in the CB and the reduced Fe ions of the photocatalyst to promote CO_2 adsorption and dissociation, leading to the formation of reactive oxygen species, methane, and CO. The reactive oxygen species reacted with the *trans*-β-methylstyrene adsorbed on the Fe@f-gC_3N_4 through coordination of the C=C bond, generating the epoxide intermediate. The subsequent ring opening of the epoxide intermediate yielded a dioxygen intermediate, which underwent C–C

bond cleavage, forming benzaldehyde and acetaldehyde. Final oxidation by the reactive oxygen species converted benzaldehyde and acetaldehyde into the obtained products, benzoic acid and acetic acid.

Conclusions

We have developed a Fe-based heterogeneous photocatalytic system that enables the selective oxidative cleavage of alkenes, using CO_2 as the sole oxygen source under mild conditions. This strategy not only provided a safer alternative to conventional oxidative cleavage methods but also demonstrates an approach for CO_2 utilization beyond its traditional role as a C_1 feedstock. Key mechanistic studies, including $C^{18}O_2$-labeling experiments and QM calculations, provided direct evidence for CO_2 splitting and oxygen transfer, thereby highlighting the feasibility of this approach. Given the fundamental importance of oxidative transformations in organic synthesis and the growing urgency of carbon capture and utilization, this work offers a promising avenue for integrating photocatalysis with sustainable oxidation strategies. We anticipate that the presented concept will serve as a guideline for future advancements in CO_2-driven oxidation reactions.

REFERENCES AND NOTES

1. Z. Guo *et al.*, Recent advances in heterogeneous selective oxidation catalysis for sustainable chemistry. *Chem. Soc. Rev.* **43**, 3480–3524 (2014). doi: 10.1039/c3cs60282f; pmid: 24553414
2. H. Baumann *et al.*, Natural fats and oils—Renewable raw materials for the chemical industry. *Angew. Chem. Int. Ed.* **27**, 41–62 (2003). doi: 10.1002/anie.198800411
3. S. Caron, R. W. Dugger, S. G. Ruggeri, J. A. Ragan, D. H. B. Ripin, Large-scale oxidations in the pharmaceutical industry. *Chem. Rev.* **106**, 2943–2989 (2006). doi: 10.1021/cr040679f; pmid: 16836305
4. Z. Hassan, M. Stahlberger, N. Rosenbaum, S. Bräse, Criegee intermediates beyond ozonolysis: Synthetic and mechanistic insights. *Angew. Chem. Int. Ed.* **60**, 15138–15152 (2021). doi: 10.1002/anie.202014974; pmid: 33283439
5. M. Rossi *et al.*, Sustainable drug discovery of multi-target-directed ligands for alzheimer's disease. *J. Med. Chem.* **64**, 4972–4990 (2021). doi: 10.1021/acs.jmedchem.1c00048; pmid: 33829779
6. B. R. Travis, R. S. Narayan, B. Borhan, Osmium tetroxide-promoted catalytic oxidative cleavage of olefins: An organometallic ozonolysis. *J. Am. Chem. Soc.* **124**, 3824–3825 (2002). doi: 10.1021/ja017295g; pmid: 11942807
7. K. Salzmann, C. Segarra, M. Albrecht, Donor-flexible bis(pyridylidene amide) ligands for highly efficient ruthenium-catalyzed olefin oxidation. *Angew. Chem. Int. Ed.* **59**, 8932–8936 (2020). doi: 10.1002/anie.202002014; pmid: 32100371
8. P. Spannring, P. C. A. Bruijnincx, B. M. Weckhuysen, R. J. M. Klein Gebbink, Transition metal-catalyzed oxidative double bond cleavage of simple and bio-derived alkenes and unsaturated fatty acids. *Catal. Sci. Technol.* **4**, 2182 (2014). doi: 10.1039/c3cy01095c
9. C. Wang, J. Xiao, Activation of molecular oxygen and selective oxidation with metal complexes. *Acc. Chem. Res.* **58**, 714–731 (2025). doi: 10.1021/acs.accounts.4c00731; pmid: 39982136
10. Y. Deng *et al.*, Disulfide-catalyzed visible-light-mediated oxidative cleavage of C=C bonds and evidence of an olefin-disulfide charge-transfer complex. *Angew. Chem. Int. Ed.* **56**, 832–836 (2017). doi: 10.1002/anie.201607948; pmid: 27936294
11. Z. Huang *et al.*, Oxidative cleavage of alkenes by O_2 with a non-heme manganese catalyst. *J. Am. Chem. Soc.* **143**, 10005–10013 (2021). doi: 10.1021/jacs.1c05757; pmid: 34160220
12. Z. Cheng *et al.*, Catalytic remodeling of complex alkenes to oxonitriles through C=C double bond deconstruction. *Science* **387**, 1083–1090 (2025). doi: 10.1126/science.adq8918; pmid: 40048532
13. European Industrial Gases Association, Fire hazards of oxygen and oxygen-enriched atmospheres (EIGA, doc 04/18, 2018); https://www.eiga.eu/uploads/documents/DOC004.pdf.
14. A. Ruffoni, C. Hampton, M. Simonetti, D. Leonori, Photoexcited nitroarenes for the oxidative cleavage of alkenes. *Nature* **610**, 81–86 (2022). doi: 10.1038/s41586-022-05211-0; pmid: 35998666
15. D. E. Wise *et al.*, Photoinduced oxygen transfer using nitroarenes for the anaerobic cleavage of alkenes. *J. Am. Chem. Soc.* **144**, 15437–15442 (2022). doi: 10.1021/jacs.2c05648; pmid: 35930615
16. F. Le Vaillant *et al.*, Catalytic synthesis of phenols with nitrous oxide. *Nature* **604**, 677–683 (2022). doi: 10.1038/s41586-022-04516-4; pmid: 35478236
17. H. Seo, M. H. Katcher, T. F. Jamison, Photoredox activation of carbon dioxide for amino acid synthesis in continuous flow. *Nat. Chem.* **9**, 453–456 (2017). doi: 10.1038/nchem.2690; pmid: 28430203
18. J. H. Ye, T. Ju, H. Huang, L. L. Liao, D. G. Yu, Radical carboxylative cyclizations and carboxylations with CO_2. *Acc. Chem. Res.* **54**, 2518–2531 (2021). doi: 10.1021/acs.accounts.1c00135; pmid: 33956436
19. W. Xiao, J. Zhang, J. Wu, Recent advances in reactions involving carbon dioxide radical anion. *ACS Catal.* **13**, 15991–16011 (2023). doi: 10.1021/acscatal.3c04125
20. R. Cauwenbergh, V. Goyal, R. Maiti, K. Natte, S. Das, Challenges and recent advancements in the transformation of CO_2 into carboxylic acids: Straightforward assembly with homogeneous 3d metals. *Chem. Soc. Rev.* **51**, 9371–9423 (2022). doi: 10.1039/D1CS00921D; pmid: 36305783
21. L. Piccirilli *et al.*, Versatile CO_2 hydrogenation-dehydrogenation catalysis with a Ru-PNP/ionic liquid system. *J. Am. Chem. Soc.* **145**, 5655–5663 (2023). doi: 10.1021/jacs.2c10399; pmid: 36867088
22. Q. Liu, L. Wu, R. Jackstell, M. Beller, Using carbon dioxide as a building block in organic synthesis. *Nat. Commun.* **6**, 5933 (2015). doi: 10.1038/ncomms6933; pmid: 25600683
23. Y. Qin *et al.*, Straightforward synthesis of functionalized γ-Lactams using impure CO_2 stream as the carbon source. *Nat. Commun.* **14**, 7604 (2023). doi: 10.1038/s41467-023-43289-w; pmid: 37989749
24. P. K. Sahoo, Y. Zhang, S. Das, CO_2-promoted reactions: An emerging concept for the synthesis of fine chemicals and pharmaceuticals. *ACS Catal.* **11**, 3414–3442 (2021). doi: 10.1021/acscatal.0c05681
25. J. Wu, Y. Huang, W. Ye, Y. Li, CO_2 reduction: From the electrochemical to photochemical approach. *Adv. Sci.* **4**, 1700194 (2017). doi: 10.1002/advs.201700194; pmid: 29201614
26. T. Y. Takeshita, B. A. Lindquist, T. H. Dunning Jr., Insights into the electronic structure of ozone and sulfur dioxide from generalized valence bond theory: Bonding in O_3 and SO_2. *J. Phys. Chem. A* **119**, 7683–7694 (2015). doi: 10.1021/acs.jpca.5b00998; pmid: 26068052
27. Z. Lu, Y. C. Chang, Q. Z. Yin, C. Y. Ng, W. M. Jackson, Photochemistry. Evidence for direct molecular oxygen production in CO_2 photodissociation. *Science* **346**, 61–64 (2014). doi: 10.1126/science.1257156; pmid: 25278605
28. H. Xu *et al.*, Oxygen harvesting from carbon dioxide: Simultaneous epoxidation and CO formation. *Chem. Sci.* **12**, 13373–13378 (2021). doi: 10.1039/D1SC04209B; pmid: 34777755
29. W. Li *et al.*, Artificial carbon neutrality through aprotic CO_2 splitting. *Angew. Chem. Int. Ed.* **64**, e202422888 (2025). doi: 10.1002/anie.202422888; pmid: 40035426
30. F. Goettmann, A. Thomas, M. Antonietti, Metal-free activation of CO_2 by mesoporous graphitic carbon nitride. *Angew. Chem. Int. Ed.* **46**, 2717–2720 (2007). doi: 10.1002/anie.200603478; pmid: 17330906
31. H. Qi *et al.*, Water-promoted carbon-carbon bond cleavage employing a reusable Fe single-atom catalyst. *Angew. Chem. Int. Ed.* **62**, e202311913 (2023). doi: 10.1002/anie.202311913; pmid: 37681485
32. C. Copéret *et al.*, Surface organometallic and coordination chemistry toward single-site heterogeneous catalysts: Strategies, methods, structures, and activities. *Chem. Rev.* **116**, 323–421 (2016). doi: 10.1021/acs.chemrev.5b00373; pmid: 26741024
33. T. Hartman, R. G. Geitenbeek, G. T. Whiting, B. M. Weckhuysen, Operando monitoring of temperature and active species at the single catalyst particle level. *Nat. Catal.* **2**, 986–996 (2019). doi: 10.1038/s41929-019-0352-1
34. A. E. Nieuwelink *et al.*, High-throughput activity screening and sorting of single catalyst particles with a droplet microreactor using dielectrophoresis. *Nat. Catal.* **4**, 1070–1079 (2021). doi: 10.1038/s41929-021-00718-7
35. A. Wang, J. Li, T. Zhang, Heterogeneous single-atom catalysis. *Nat. Rev. Chem.* **2**, 65–81 (2018). doi: 10.1038/s41570-018-0010-1
36. X. Shi *et al.*, Metal-support frontier orbital interactions in single-atom catalysis. *Nature* **640**, 668–675 (2025). doi: 10.1038/s41586-025-08747-z; pmid: 40175541
37. I. Ghosh *et al.*, Organic semiconductor photocatalyst can bifunctionalize arenes and heteroarenes. *Science* **365**, 360–366 (2019). doi: 10.1126/science.aaw3254; pmid: 31346061
38. S. Ji *et al.*, Chemical synthesis of single atomic site catalysts. *Chem. Rev.* **120**, 11900–11955 (2020). doi: 10.1021/acs.chemrev.9b00818; pmid: 32242408
39. W. J. Ong, L. L. Tan, Y. H. Ng, S. T. Yong, S. P. Chai, Graphitic carbon nitride ($g\text{-}C_3N_4$)-based photocatalysts for artificial photosynthesis and environmental remediation: Are we a step closer to achieving sustainability? *Chem. Rev.* **116**, 7159–7329 (2016). doi: 10.1021/acs.chemrev.6b00075; pmid: 27199146
40. S. Bhunia, A. Ghatak, A. Dey, Second sphere effects on oxygen reduction and peroxide activation by mononuclear iron porphyrins and related systems. *Chem. Rev.* **122**, 12370–12426 (2022). doi: 10.1021/acs.chemrev.1c01021; pmid: 35404575
41. X. Chen, J. Zhang, X. Fu, M. Antonietti, X. Wang, $Fe\text{-}g\text{-}C_3N_4$-catalyzed oxidation of benzene to phenol using hydrogen peroxide and visible light. *J. Am. Chem. Soc.* **131**, 11658–11659 (2009). doi: 10.1021/ja903923s; pmid: 19642702
42. W. Nam, High-valent iron(IV)-oxo complexes of heme and non-heme ligands in oxygenation reactions. *Acc. Chem. Res.* **40**, 522–531 (2007). doi: 10.1021/ar700027f; pmid: 17469792
43. B. Meunier, Metalloporphyrins as versatile catalysts for oxidation reactions and oxidative DNA cleavage. *Chem. Rev.* **92**, 1411–1456 (1992). doi: 10.1021/cr00014a008
44. Z. Chen *et al.*, Splitting CO_2 into CO and O_2 by a single catalyst. *Proc. Natl. Acad. Sci. U.S.A.* **109**, 15606–15611 (2012). doi: 10.1073/pnas.1203122109; pmid: 22685210

45. T. Kong, Y. Jiang, Y. Xiong, Photocatalytic CO_2 conversion: What can we learn from conventional CO_x hydrogenation? *Chem. Soc. Rev.* **49**, 6579–6591 (2020). doi: 10.1039/C9CS00920E; pmid: 32789318
46. J. Schneider, H. Jia, J. T. Muckerman, E. Fujita, Thermodynamics and kinetics of CO_2, CO, and H^+ binding to the metal centre of CO_2 reduction catalysts. *Chem. Soc. Rev.* **41**, 2036–2051 (2012). doi: 10.1039/C1CS15278E; pmid: 22167246
47. P. Ren *et al.*, An atomically dispersed Mn-photocatalyst for generating hydrogen peroxide from seawater via the water oxidation reaction (WOR). *J. Am. Chem. Soc.* **145**, 16584–16596 (2023). doi: 10.1021/jacs.3c03785; pmid: 37487055
48. P. K. Sahoo *et al.*, An atomically dispersed Mn photocatalyst for vicinal dichlorination of nonactivated alkenes. *J. Am. Chem. Soc.* **147**, 11829–11840 (2025). doi: 10.1021/jacs.4c16413; pmid: 40130771
49. T. Zhang *et al.*, Atomic-level understanding for the enhanced generation of hydrogen peroxide by the introduction of an aryl amino group in polymeric carbon nitrides. *ACS Catal.* **11**, 14087–14101 (2021). doi: 10.1021/acscatal.1c03733
50. E. Murphy *et al.*, Synergizing Fe_2O_3 nanoparticles on single atom Fe-N-C for nitrate reduction to ammonia at industrial current densities. *Adv. Mater.* **36**, 2401133 (2024). doi: 10.1002/adma.202401133; pmid: 38619914
51. S. Ding *et al.*, Effect of phosphorus modulation in iron single-atom catalysts for peroxidase mimicking. *Adv. Mater.* **36**, 2209633 (2024). doi: 10.1002/adma.202209633; pmid: 36722360
52. Y. Deng *et al.*, Atomic Fe-doped MOF-derived carbon polyhedrons with high active-center density and ultra-high performance toward PEM fuel cells. *Adv. Energy Mater.* **9**, 1802856 (2019). doi: 10.1002/aenm.201802856
53. Y. Zhou *et al.*, Fe-N-C electrocatalysts with densely accessible Fe-N_4 sites for efficient oxygen reduction reaction. *Adv. Funct. Mater.* **31**, 2102420 (2021). doi: 10.1002/adfm.202102420
54. S. Ni, D. Spinnato, J. Cornella, Reductive cyclopropanation through bismuth photocatalysis. *J. Am. Chem. Soc.* **146**, 22140–22144 (2024). doi: 10.1021/jacs.4c07262; pmid: 39102564
55. T. Ghosh *et al.*, A robust Fe-based heterogeneous photocatalyst for the visible-light-mediated selective reduction of an impure CO_2 stream. *Chem. Sci.* **15**, 11488–11499 (2024). doi: 10.1039/D4SC02773F; pmid: 39055026
56. Y. Gao, M. Pink, V. Carta, J. M. Smith, Ene reactivity of an Fe=NR bond enables the catalytic α-deuteration of nitriles and alkynes. *J. Am. Chem. Soc.* **144**, 17165–17172 (2022). doi: 10.1021/jacs.2c07462; pmid: 36070477
57. H. A. Obeid, J. Hannedouche, Iron-catalyzed positional and geometrical isomerization of alkenes. *Adv. Synth. Catal.* **365**, 1100–1111 (2023). doi: 10.1002/adsc.202300052
58. M. Alves *et al.*, Organocatalyzed coupling of carbon dioxide with epoxides for the synthesis of cyclic carbonates: Catalyst design and mechanistic studies. *Catal. Sci. Technol.* **7**, 2651–2684 (2017). doi: 10.1039/C7CY00438A

ACKNOWLEDGMENTS

G. V. and X. H. thank N. Allasia (Politecnico di Milano), S. Palit (Politecnico di Milano), T. A. Gazis (Politecnico di Milano), and A. Maximenko (SOLARIS) for their valuable assistance during synchrotron experiments. **Funding:** We are highly thankful to the UBT for start-up funding and generous support. We are also grateful for DTU grant 2035-00147B. P.R. gratefully acknowledges the financial support from the Taiyuan University of Science and Technology Scientific Research Initial Funding (no. 20252080). A.K. gratefully acknowledges support by the Bavarian State Ministry of Science, Research, and Arts through the grant Solar Technologies go Hybrid (SolTech). G.V. and X.H. gratefully acknowledge access to the National Synchrotron Radiation Centre SOLARIS, where the x-ray absorption spectroscopy data were collected (proposal 233216). XAS measurements were supported by the Polish Ministry of Science and Higher Education under the project "Support for research and development using the research infrastructure of the National Synchrotron Radiation Centre SOLARIS" (contract no. 1/SOL/2021/2). Further development of the ASTRA beamline at SOLARIS for low-photon energy measurements was funded through the EU Horizon 2020 program (grant no. 952148 – Sylinda). The XPS measurements were carried out with the equipment purchased thanks to the financial support of the Smart Growth Operational Programme (contract no. POIR.04.02.00-00-D001/20). The financial support of the Strategic Programme Excellence Initiative at Jagiellonian University, used for servicing measurement systems, is also appreciated. **Author contributions:** Conceptualization: S.D., M.B., Y.Q.; Investigation: Y.Q., S.P., T.H.V., J.R., X.H., L.A., G.V., N.R., S.M., G.B., A.J., P.K., D.H., J.B., S.B., A.K.; Methodology: Y.Q., P.R., J.H.; Supervision: S.D., M.B.; Writing – original draft: Y.Q., S.D.; Writing – review & editing: Y.Q., S.D., M.B. **Competing interests:** The authors declare that they have no competing interests. **Data, code, and materials availability:** All data are available in the main text or the supplementary materials, as are details for the synthesis of all reported compounds.

SUPPLEMENTARY MATERIALS

science.org/doi/10.1126/science.aed6068
Materials and Methods; Supplementary Text; Figs. S1 to S47; Tables S1 to S7; Spectral Data; References (*59*–*94*)

Submitted 3 November 2025; accepted 17 March 2026

10.1126/science.aed6068

Photocatalyzed oxidative cleavage of alkenes using CO_2 as an oxygen donor

Yuman Qin, Peng Ren, Jun Hu, Suman Pradhan, Thanh Huyen Vuong, Xiufang He, Lulu Alluhaibi, Nils Rockstroh, Susanna Monti, Giovanni Barcaro, Aleksander Jaworski, Piotr Ku#trowski, Jabor Rabeah, Daniel Hohenberger, Sergey Bagnich, Anna Köhler, Josef Breu, Gianvito Vilé, Matthias Beller, and Shoubhik Das

Science **392** (6802), eaed6068. DOI: 10.1126/science.aed6068

Editor's summary

Slicing through carbon-carbon double bonds is a job for strong oxidants. Typical reagents include ozone and high-valent metal oxides. Carbon dioxide is essentially the thermodynamic opposite of those oxidants and conventionally reacts at the carbon rather than either oxygen. Remarkably, Qin *et al*. nonetheless found that a heterogeneous iron photocatalyst can break alkenes into ketones and acids using the oxygen from carbon dioxide. Hydrogen donation by chloroform assists the process, which appears to occur through an epoxide intermediate. —Jake S. Yeston

Science (ISSN 1095-9203) is published by the American Association for the Advancement of Science. 1200 New York Avenue NW, Washington, DC 20005. The title *Science* is a registered trademark of AAAS.